

Structural, optical properties, impedance spectroscopy studies and electrical conductivity of SnO₂ nanoparticles prepared by polyol method

Wissem Ben Soltan¹ · Saber Nasri² · Mohamed Saber Lassoued^{1,3} · Salah Ammar^{1,4}

Received: 27 October 2016 / Accepted: 6 January 2017 / Published online: 19 January 2017
© Springer Science+Business Media New York 2017

Abstract Tin oxide nanoparticles (SnO₂) with controlled shapes and sizes were prepared at 160 °C by a simple polyol method. The formation of typical rutile-type was confirmed by X-ray diffraction studies, and it was found to be a tetragonal structure. X-ray diffraction and transmission electron microscopy show the average diameter of SnO₂ nanoparticles about 13 nm obtained after calcination at 700 °C. Moreover, the calcined sample is composed of an aggregated network of almost spherical nanoparticles. The optical property was investigated using an UV–visible Diffuse Reflectance Spectroscopy, the band gap is found to be 3.4 eV. Electrical properties were performed using impedance spectroscopy technique in the frequency range 6 KHz–1 MHz at various temperatures (523–723 K). The complex impedance diagram at different temperatures showed a single semicircle, implying that the response originated from a single capacitive element corresponding to the grains. Ac and dc conductivities were studied to explore the mechanisms of conduction. In fact, AC conductivity is found to follow Jonsche's universal power law. As a result, the exponent's was found to increase with increase in temperature. Further analysis revealed that, the

non overlapping small polaron tunneling model mechanism was applicable at the present temperatures.

1 Introduction

Nanometer-sized materials have attracted a considerable amount of attention due to their unique chemical, physical, electrical and magnetic properties; these materials behave differently from bulk semiconductors. In recent years there has been a growing interest in the use of transparent conducting oxide thin powder as conducting solar window materials in thin film solar cells [1], various gas sensors [2] and heat reflectors for advanced glazing in solar applications [3].

Among these materials, tin oxide (SnO₂) has a tetragonal structure, similar to the rutile structure, is sought for a variety of application, and behaves as an n type semiconductor having band gap (3.6 eV). The SnO₂ nanomaterials used as gas sensors [4], dye-sensitized solar cells [1, 5], lithium rechargeable batteries [6] and photocatalytic degradation of organic dyes [7], depends strongly on its size and morphology. SnO₂ nanostructures, including nanoparticles [8], nanowires [9], nanobelts [10], nanorods [11], microporous and mesoporous structures [12, 13]. The SnO₂ nanoparticles have been synthesized by a variety of methods such as polyol method [14–16], sol–gel method [17], hydrothermal method [18–20], co-precipitation [21], solvothermal method [22], spray pyrolysis [23] and physical vapor deposition [24].

In the present work, we have used the polyol method to synthesize the SnO₂ nanoparticles. The polyol method is particularly attractive due to its short preparation time, low cost, high purity and the ability to control the grain size. The prepared nanoparticles were analyzed by X-ray

✉ Wissem Ben Soltan
wissemdocsoltan@hotmail.fr

¹ Département de chimie, Faculté des Sciences de Gabès, Cité Erriadh, Université de Gabès, 6072 Gabès, Tunisia

² Condensed Matter Laboratory, Faculty of Sciences, University of Sfax, PB 1171, 3000 Sfax, Tunisia

³ Laboratoire des Sciences des Matériaux et de l'Environnement, Faculté des Sciences de SFAX, Université de Sfax, PB 1171, 3000 Sfax, Tunisia

⁴ Département de chimie, Faculté des Sciences de Bizerte, Université de Carthage, Bizerte, Tunisia

diffraction analysis (XRD), UV–visible Diffuse Reflectance Spectroscopy, transmission electron microscopy (TEM) and dielectric studies.

On the other hand, the dielectric relaxation phenomenon shows important effect on the electrical properties of the capacitors, since the leakage current behavior under electric fields used in actual device operation is attributed to the dielectric relaxation. Therefore, knowledge of the dielectric properties in semiconducting materials is very important for the development of devices in microelectronics. AC measurements are important for studying the dynamic properties (dielectric loss, capacitance and conductance) of the semiconducting and dielectric materials.

They provide information about interior of the materials in the region of relatively low conductivity. This measurement also helps to distinguish between localized and free band conduction. In the case of localized conduction, the AC conductivity increases with frequency while the free band conduction the conductivity decreases with frequency.

In this paper, we report an analysis of the structural and AC conductivity of the compounds SnO₂.

2 Experimental procedure

Tin dioxide nanoparticles were synthesized by a polyol-based method using tin (IV) tetrachloride pentahydrate 0.15 M (SnCl₄·5H₂O, 98%, Aldrich) as tin source. The precursor was first dissolved in 50 ml of DEG (Diethylene glycol, 99%, Aldrich). On the other hand, sodium acetate (CH₃COONa·3H₂O) was dissolved in 75 ml of DEG, which is used as precipitating agent. Finally, when the solution temperature tin precursor reaches 120 °C, we added drop wise the solution of the sodium acetate in the three-necked flask using a dropping funnel. The mixture was further heated at 160 °C for 7 h yielding a white precipitate. After cooling to room temperature, the resulting precipitate was then collected by centrifugation, washed several times with water and ethanol. The resulting products were dried at 90 °C for 24 h and then calcined at 700 °C for 8 h to obtain the final SnO₂ nanoparticles.

X-ray diffraction (XRD) studies were recorded on a Bruker AXS diffractometer (D2 PHASER A26-X1-A2B0D3A) using a Cu anode (K α radiation, $\lambda = 1.54056$ Å). Structural properties were carried out using the standard Rietveld technique [25]. A continuous scan mode was employed to collect 2θ data from 10° to 80° with a 0.02° sampling pitch and a 2° min⁻¹ scan rate. Diffuse Reflectance UV–visible properties of the nanoparticles were determined using a Shimadzu UV-3101 PC spectrophotometer equipped with an integration sphere in the 200–2000 nm wavelength range. HR-TEM images were recorded with JEOL JEM-2100 microscope after dispersing

the powders in ethanol and coating a small droplet of the suspension on holey carbon (Cu) grid.

The electrical properties of the SnO₂ nanoparticles calcined at 700 °C were determined using impedance spectroscopy (IS) technique. The latter is indeed a powerful tool for characterizing many of the electrical properties of materials and their interfaces [26]. In our case, the polycrystalline sample was pressed into pellets of 8 mm diameter and 1.2 mm thickness using 3 t/cm² uniaxial pressures. Electrical impedances were measured in the frequency range from 209 Hz to 5 MHz with TEGAM 3550 ALFred automatic bridge and in the temperature range between 543 and 723 K.

3 Results and discussions

3.1 Structural studies

Figure 1 displays XRD patterns of the calcined SnO₂ sample and shows a pure crystalline phase with broad diffraction peaks corresponding to a rutile structure with P42/mnm space group. No characteristic peaks of other impurities were observed, indicating that the product has a good crystallinity and purity.

The Rietveld refinement of the X-ray data of our sample, were carried out using the FULLPROF code [25, 27]. The results are reported in Fig. 1, we displayed X-ray diffraction refinement at room temperature.

The quality of refinement was evaluated through the goodness of the fit indicator χ^2 , such as $\chi^2 = 1.6344$ and refinement factors $R_F = 4.1501$. A good agreement between the calculated and experimental spectra is obtained with the

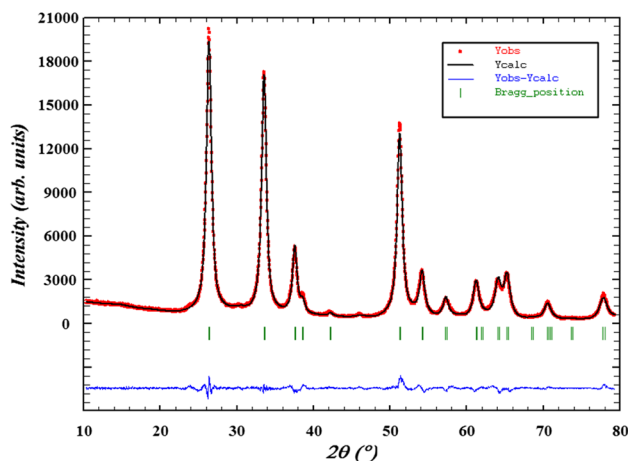


Fig. 1 Observed and calculated X-ray diffraction data and Rietveld refinement for SnO₂. Vertical bars are the Bragg reflections. The difference pattern between the observed data and fits is shown at the bottom

parameters $R_p = 7.67$, $R_{wp} = 9.65$ and $R_{exp} = 7.55$. Rietveld refinement showed that the lattice parameters of the unit cell $a=b=4,7524 \text{ \AA}$, $c=3,1961 \text{ \AA}$ and The volume of the unit cell $V=72,1848 \text{ \AA}^3$ for pure SnO_2 which are in good agreement with the literature (Joint Committee on Powder Diffraction Standards card no. 41-1445) [28–30]. The unit cell contains six atoms. Each tin ion Sn^{4+} , is at the center of an almost regular octahedron formed by six oxygen ions, while each O^{2-} is surrounded by three Sn^{4+} located at the vertices of an isosceles triangle. The distance two bonds in SnO_2 are $2 \times 2.035 \text{ \AA}$ and $4 \times 2.065 \text{ \AA}$ (See Fig. 2). Similar results were found by Khaled Melghit and Khalid Bouziane [31]. The average crystallite size D of our compounds was deduced from full width at half maximum (FWHM) according to Scherrer’s formula:

$$D = \frac{0.9}{\beta \cos \theta} \tag{1}$$

where λ , θ , and β are the X-ray wavelength, the Bragg diffraction angle, and the full width at half- maximum of the diffraction peak (FWHM), respectively. The average

crystallite size as determined from the main XRD peak (110) is found to be around $12.8 \pm 1.2 \text{ nm}$.

The morphology and the particle size were then studied by TEM analysis. Figure 3 shows the TEM micrograph of SnO_2 nanoparticles calcined at $700 \text{ }^\circ\text{C}$, and shows agglomerated, nearly spherical particles with an average size of about $12.5 \pm 0.5 \text{ nm}$. It is worth mentioning that this value was in good agreement with the mean crystallite size deduced from the Scherrer relationship which indicates that the nanoparticles are well-crystallized.

3.2 Optical properties

The optical properties of SnO_2 nanopowders after calcination were investigated by Diffuse Reflectance UV–visible spectroscopy (DRS). The absorption spectra of tin oxide in the UV and visible range are depicted in Fig. 4a. Each spectrum exhibits an intense absorption in the 200–420 nm wavelength range and an absorption edge between 300 and 370 nm [15].

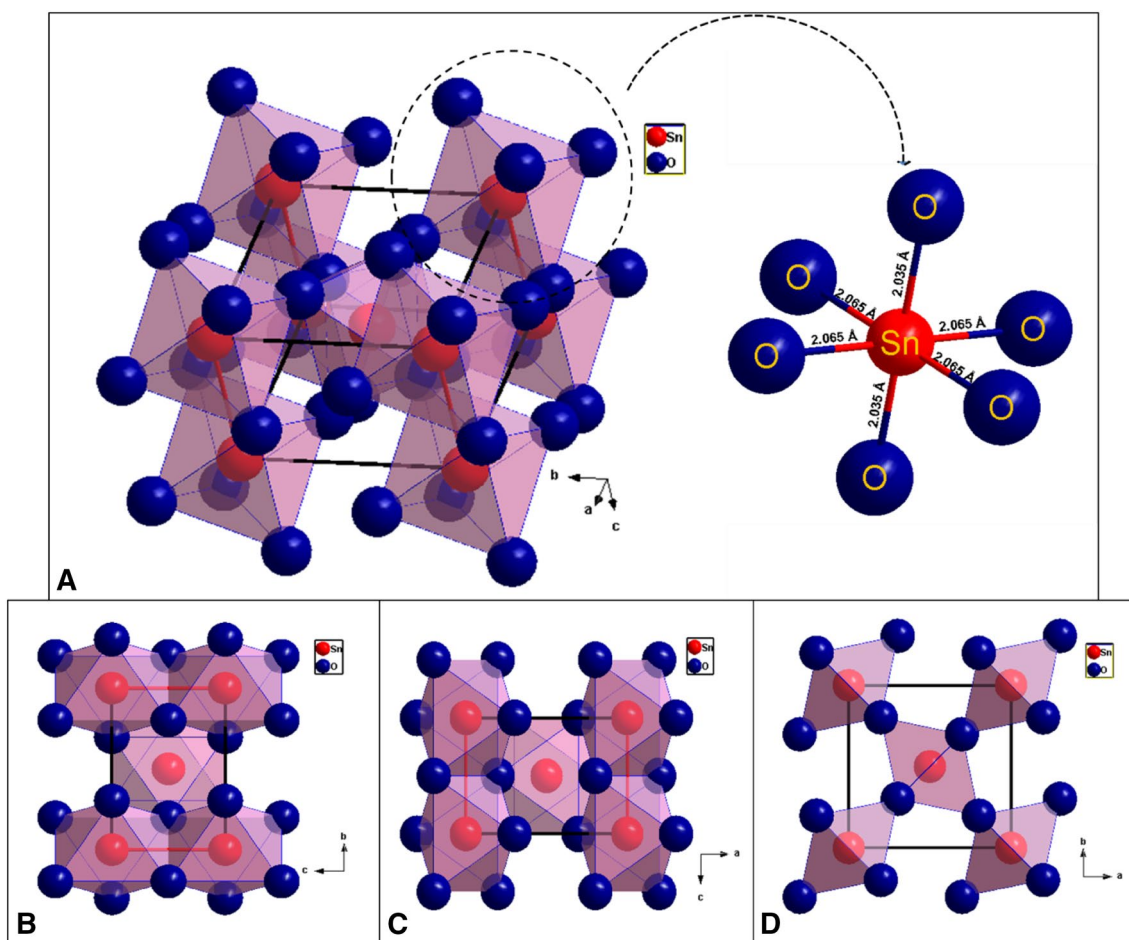


Fig. 2 The crystal structures of SnO_2

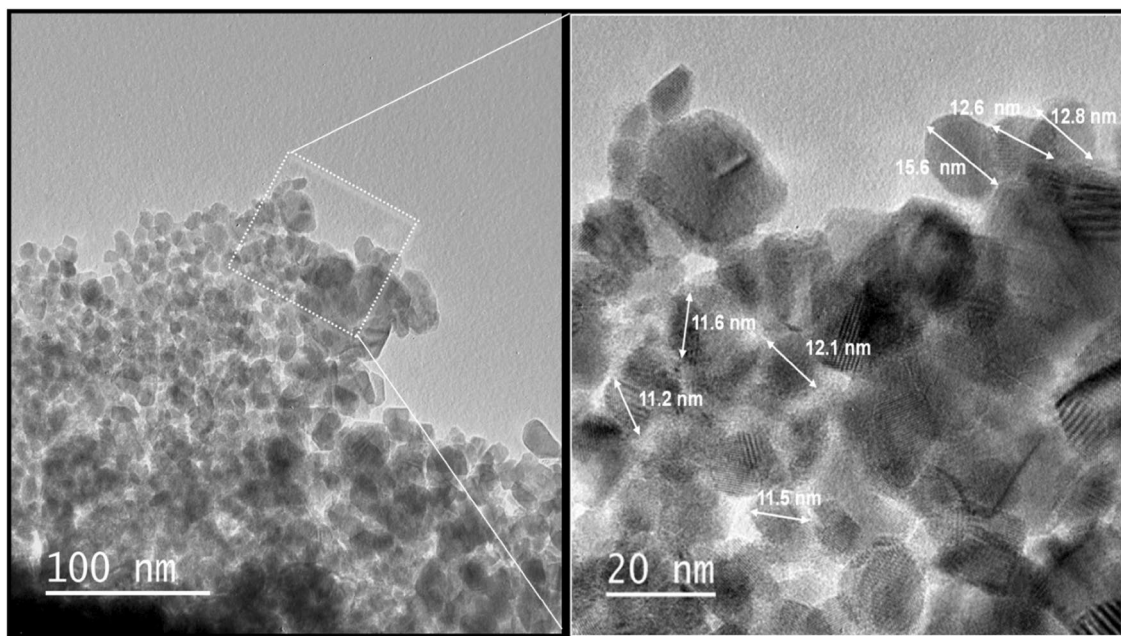


Fig. 3 TEM images of SnO₂ nanoparticles

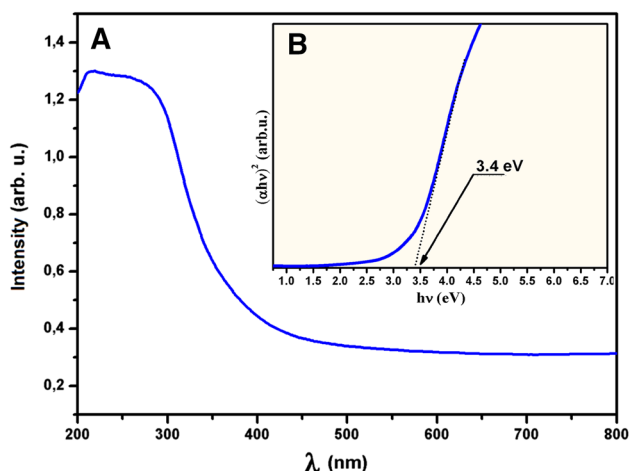


Fig. 4 **a** UV–visible absorption spectra of SnO₂ nanoparticles **b** Plot of $(\alpha h\nu)^2$ versus photon energy ($h\nu$) of SnO₂ nanoparticles. The inset shows the band gap energy (E_g)

To obtain a more quantitative estimation of this trend, property of nanoparticles, the band gap energy (E_g) of the samples prepared was deduced from their absorption spectra by using the following Eq. (2) [32]:

$$\alpha(h\nu) = A(h\nu - E_g)^n \quad (2)$$

where α , ν , E_g , A and n are the absorption coefficient (or optical density), light frequency, band gap energy, a constant and a parameter depending on the nature of the semiconductor, respectively. As cassiterite SnO₂ is a direct

semiconductor [33], the optical band gap energies of the as-synthesized samples for direct transition ($n=1/2$) can thus be estimated from a plot of $(\alpha h\nu)^2$ versus $h\nu$, the intercept between the linear part of fit with x-axis gives the value of the value of the band gap energy (E_g) of the material. When $(\alpha h\nu)^2$ is zero, the photon energy is E_g . As it can be seen from Fig. 4B, the band gap energy estimated about at 3.4 eV, the results obtained are similar to those found by Bargougui et al. [34].

3.3 Impedance studies

The complex impedance spectroscopic (CIS) technique is used to evaluate the electrical response of materials in a wide range of frequencies and temperature. It is the most frequently used technique to investigate the dielectric behavior and dynamics of the ionic movement in electrical materials [35]. In fact, this technique is extremely useful in determining the contribution of different mechanisms in conduction process and differentiating the transport characteristics in grain boundaries [36]. The complex impedance spectroscopy is a powerful tool to analyze the microstructure and properties relationship. Thus, the physical process occurring inside the sample can be modeled as an equivalent circuit using impedance spectra.

Shown in Fig. 5a, b are the complex impedance plane plots of the tin oxide nanoparticles (SnO₂) at different temperatures. One semi-circular arcs is observed for all temperatures related to the bulk effects. Generally, the contribution of various microscopic elements such as bulk,

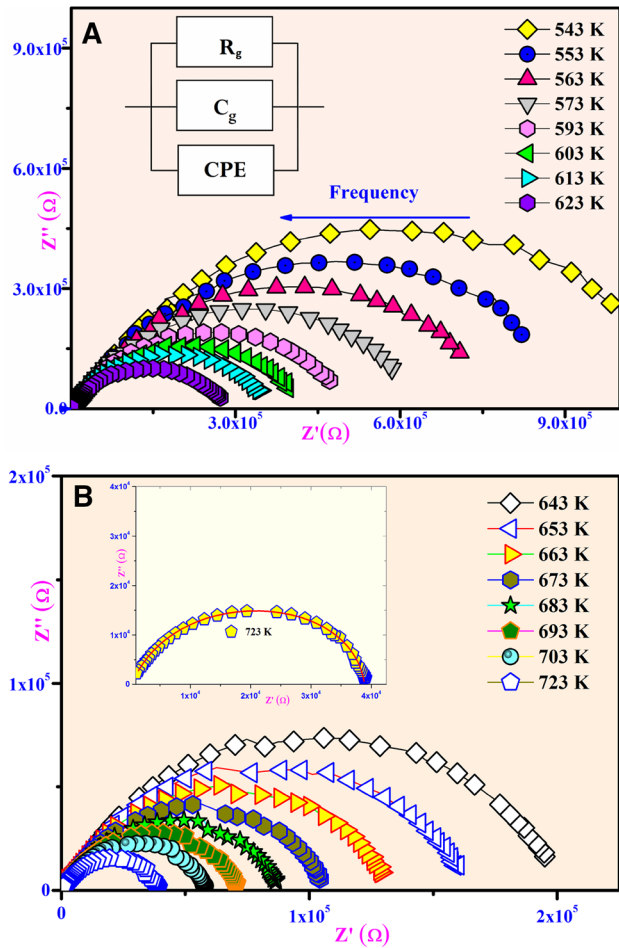


Fig. 5 a, b Complex impedance spectrum in the Nyquist plane with electrical equivalent circuit (inset), accompanied by theoretical data

grain boundary, and electrodes to total electric response in polycrystalline materials can be modeled by the reference to an equivalent circuit. In the present case, the impedance results were analyzed using ZView software. The inset in Fig. 5a shows the equivalent circuit used to represent electrical properties of the material. Thus, a best fit was obtained when we use an equivalent circuit contains a parallel combination of a resistance, capacitance, and fractal capacitance (Fig. 5b inset). So, the CPE impedance is given by the relationship:

$$Z_{CPE} = \frac{1}{Q(j\omega)^\alpha} \tag{3}$$

Here α is related to the deviation from the vertical of the line in the $-Z''$ versus Z' plot.

$\alpha = 1$ indicates a perfect capacitance and lower α values directly reflect the roughness of the electrode used.

Figure 6 depicts the variation of imaginary part of impedance Z'' as a function of frequency at different temperatures for (SnO₂) sample. It's is noticed that the

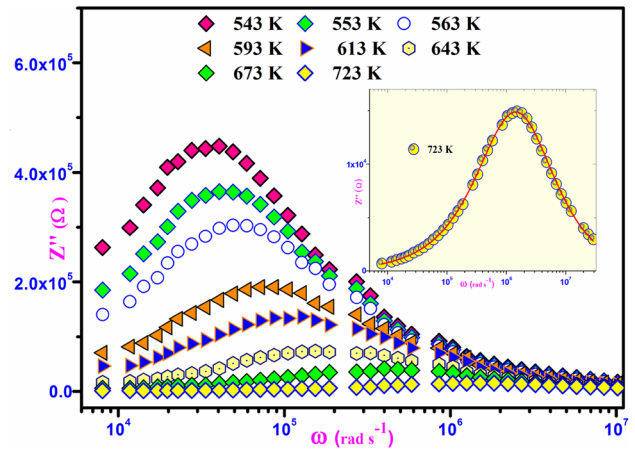


Fig. 6 Variation of imaginary part of the impedance as a function of frequency and temperature

imaginary part Z'' increases with frequency reaching a maximum peak Z'' max then decreases as the temperature increases. From the figure, Z'' max decreases as the temperature increases, in the same line the position of relaxation peak moves to higher frequencies suggest a spread of relaxation time in the system [37]. Finally, all spectra merge in the high-frequency region. In fact, this behavior is an indication of the accumulation of space charge polarization effect in the material at lower frequency and at higher temperature [38].

Figure 7 shows the dependence of the real part of the impedance Z' on the frequency at several temperatures. The existence of negative temperature coefficient of resistance (NTCR) in tin oxide nanoparticles (SnO₂) can be accounted in terms of decrement in Z' with temperature at low frequency region. The decrease of Z' is up to a certain frequency and then it remains almost constant value with the

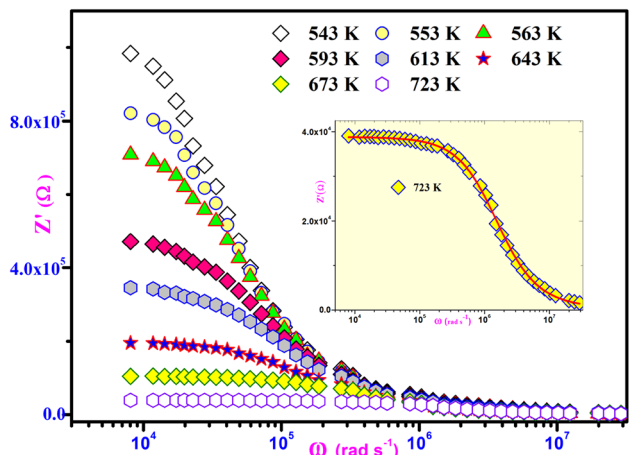


Fig. 7 Variation of real part of the impedance as a function of frequency and temperature

increase in frequency which may be due to the release of space charge polarization and reduces the barrier properties in this material [39].

In the inset of Figs. 6 and 7, respectively we represent the Z'' and Z' versus frequency at 723 K with fits to the equivalent circuit. The excellent agreement between experimental (scatter) and theoretical curve (line) indicates that the equivalent circuit describes the material electrolyte interface reasonably well. As a matter of fact, the fitted values of the circuit parameters for the different temperatures are given in Table 1. It's clear from this latter, that all the capacitance values (C) are in the range of pF corresponds to a bulk capacitance. Otherwise, the grain resistance R_g decreases with rise in temperature due to the increase of the mobility of charge carriers that adds to the conduction process.

To appreciate the relaxation phenomenon on the electrical properties of SnO_2 -NPs sample, Nyquist plots reported in Fig. 8 shows the frequency dependence of Z' and Z'' at 623 K. As the frequency rise, Z'' increases, whereas Z' decreases. This trend continues up to a particular frequency which Z'' occupies a maximum value and in Z' intersects. Furthermore, if the frequency increases both Z' and Z'' decrease and above 10^7 Hz both values merge with X-axis. This result indicates suggested that there exists a relaxation phenomenon [40]. It is evident from the figures that the peak frequency shifts toward higher frequencies and could be attributed to the dependence of the relaxation process. Additionally, the inset of Fig. 8 shows that Argand diagram (imaginary part Z'' vs. its real part Z') allows the

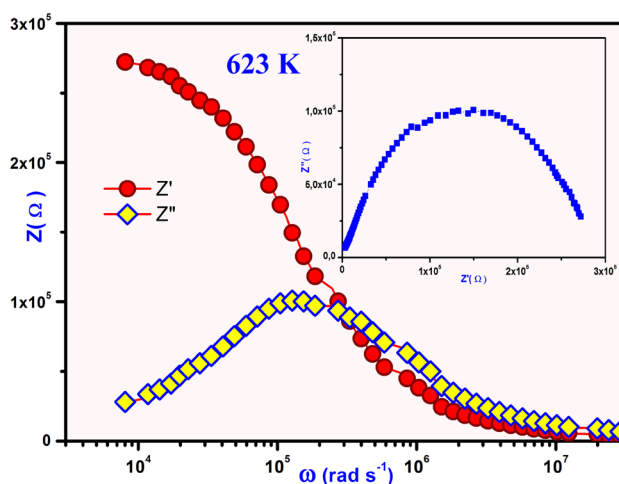


Fig. 8 Frequency dependence of Z' and Z'' for SnO_2 -NPs and Argand diagram (inset)

determination of bulk ohmic resistance as a function of temperature and thus temperature dependence of conductivity [41].

The electrical conductivity σ_{dc} was calculated from R_g by the relation, $\sigma_{dc} = \frac{e}{R_g \cdot S}$, where e and S are thickness and area of the pellet, respectively. In Fact, σ_{dc} obeys to Arrhenius law as shown in Fig. 9:

$$\sigma_{dc} T = A \exp\left(\frac{-E_a}{k_B T}\right) \tag{4}$$

where A is the pre-exponential factor, k_B is the Boltzmann constant and E_a is the activation energy. The value of E_a obtained from the least square linear fit is shown in the inset of Fig. 9.

Table 1 The equivalent circuit parameters for the nanoparticles (SnO_2)

T (K)	R_g (K Ω)	C (10^{-12} F)	Q_{gb} (10^{-10} F)	α
723	39.36	1.93	2.74	0.83
703	58.99	2.77	9.19	0.80
693	72.42	3.16	7.34	0.79
683	89.14	3.54	6.00	0.78
673	109.31	4.12	5.24	0.78
663	135.65	4.20	3.18	0.76
653	169.66	4.86	2.47	0.76
643	212.95	6.13	1.78	0.74
623	294.58	5.37	1.34	0.74
613	396.27	5.72	0.83	0.73
603	466.90	5.80	0.87	0.72
593	573.07	5.88	0.97	0.72
573	762.23	5.83	1.15	0.71
563	956.11	5.29	2.25	0.72
553	1158.30	5.15	1.73	0.72
543	1381.40	4.90	1.63	0.72

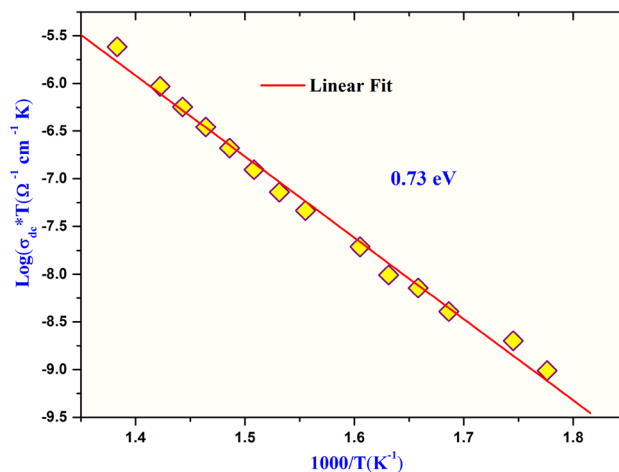


Fig. 9 Variation of $(\text{Log } \sigma_{dc} * T)$ vs. $(1000/T)$. Symbols are experimental points and solid line is the straight line fit

3.4 AC conductivity

The measurement of the ac response is a prominent factor that gives us important information about the conduction process in the materials [42]. In this way, the angular frequency dependence of the AC conductivity at different temperatures is shown in Fig. 10. It can be observed that the conductivity pattern can be flatly divided into two distinct regions. Firstly, the conductivity is found almost to be frequency-independent in low frequency region. Where random distribution of the charge carriers via activated hopping gives rise to a frequency-independent conductivity. While at high frequencies the conductivity increases gradually with the increase in frequency. The conductivity spectra become more dispersive with the rise in frequency and tend to merge in high frequency regime as the width of dispersion region decreases with increase in temperature exhibiting the weak temperature dependence. The changeover of the conductivity is shifted toward higher frequencies with increase in temperature because mobile ions procure more thermal energy and cross the barrier more readily [43]. In other words, when temperature is increased the dispersion starts at a higher frequency.

The frequency dependence of the conductivity generally obeys the Jonscher’s power-law

$$\sigma_{ac}(\omega) = \sigma_{dc} + A\omega^s \tag{5}$$

where σ_{dc} is the direct current conductivity of the sample and ω the angular frequency of measurement. The exponent s represents the degree of interaction between mobile ions and the lattices surrounding them and A is a temperature-dependent constant which determines the power of polarizability. The results of the experimental conductivity spectra fit using Eq. (5) are summarized in Table 2.

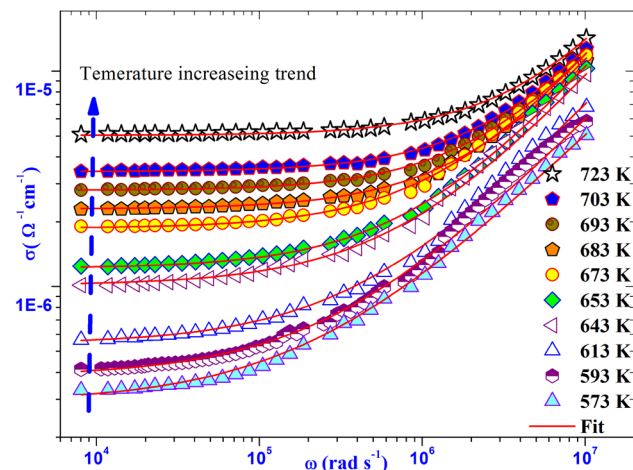


Fig. 10 Frequency dependence of AC conductivity of SnO₂ at different temperatures

Table 2 Parameters of fitting of ac conductivity with Jonscher’s universal power law

T (K)	σ_{dc} ($\Omega^{-1} \text{ cm}^{-1}$)	A	n
723	5.04E-06	1.01E-12	0.992
703	3.42E-06	1.28E-12	0.980
693	2.80E-06	1.67E-12	0.963
683	2.30E-06	1.87E-12	0.955
673	1.87E-06	4.29E-12	0.910
663	1.51E-06	4.39E-12	0.899
653	1.21E-06	5.88E-12	0.885
643	1.01E-06	8.31E-12	0.859
623	7.17E-07	1.01E-11	0.837
613	5.43E-07	1.36E-11	0.811
603	4.82E-07	1.42E-11	0.807
593	3.82E-07	2.04E-11	0.777
573	2.21E-07	2.99E-11	0.743
563	1.77E-07	5.23E-11	0.716
553	1.18E-07	6.53E-11	0.693
543	8.48E-08	6.76E-11	0.676

From another point of view, ω_h is the hopping frequency of the charge carrier that represents the crossover frequency from dc to dispersive conductivity region at $\omega > \omega_h$. It can be calculated directly from a.c conductivity data using the equation [44].

$$\omega_h = \left(\frac{\sigma_{dc}}{A} \right)^{1/s} \tag{6}$$

The temperature dependence of ω_h versus $1000/T$ is shown in Fig. 11. The corresponding activation energy value is found to be 0.78 (±0.03) eV.

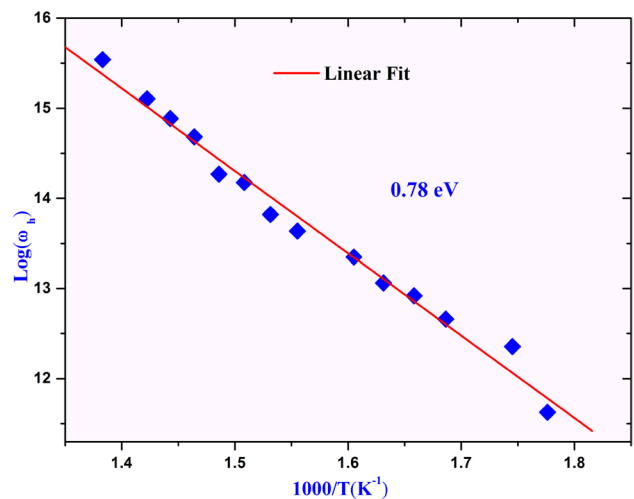


Fig. 11 The Plot of hopping frequency ω_h versus $1000/T$

4 Conclusion

Overall, in this work, tin oxide nanoparticles (SnO_2) with controlled shapes and sizes were successfully prepared a simple polyol method. The XRD analysis revealed that the crystallites have the expected SnO_2 tetragonal phase with $P_{4/2}mm$ space group. The band gap estimated about 3.4 eV. Indeed, the electrical properties studies displayed an interesting property of SnO_2 -NPs. In fact, the impedance plot has shown semi circle arcs at different temperatures and in order to explain the impedance results, an electrical equivalent circuit has been proposed. Besides, both ac and dc conduction mechanism was investigated thoroughly. Also, it has been found that, the power law exponent, s , is temperature dependent and the non overlapping of small polaron tunneling (NSPT) mechanism was found to be responsible for ac conduction process.

References

1. S. Gubbala, V. Chakrapani, V. Kumar, M.K. Sunkara, *Adv. Funct. Mater.* **18**, 2411 (2008)
2. Y. Yu, C.H. Chen, Y. Shi, *Adv. Mater.* **19**, 993 (2007)
3. J. Zhang, S.R. Wang, M.J. Xu, Y. Wang, H.J. Xia, S.M. Zhang, *J. Phys. Chem. C* **113**, 1662 (2009)
4. Z.P. Li, Q.Q. Zhao, W.L. Fan, J.H. Zhan, *Nanoscale* **3**, 1646–1652 (2011)
5. L. Cojocaru, C. Olivier, T. Toupance, E. Sellier, L. Hirsch, *J. Mater. Chem. A* **1**, 13789 (2013)
6. X.W. Lou, Y. Wang, C.L. Yuan, Y.L. Jim, A.A. Lynden, *Adv. Mater.* **18**, 2325–2329 (2006)
7. A. Bhattacharjee, M. Ahmaruzzaman, *Mater. Lett.* **139**, 418–421 (2015)
8. M. Aziz, S.S. Abbas, WRW Baharom, *Mater. Lett.* **91**, 31–34 (2012)
9. J.K. Jian, X.L. Chen, W.J. Wang, L. Dai, X.P. Xu, *Appl. Phys. A* **76**, 291–294 (2003).
10. X.L. Ma, Y. Li, Y.L. Zhu, *Chem. Phys. Lett.* **376**, 794–798 (2003)
11. B. Cheng, M.R. Joette, W.S. Shi, L. Zhang, T.S. Edward, *J. Am. Chem. Soc.* **126**, 5972–5973 (2004)
12. T. Hyodo, S. Abe, Y. Shimizu, M. Egashira, *Sens. Actuators B* **93**, 590–600 (2003)
13. G.C. Xi, Y.T. He, Q. Zhang, H.Q. Xiao, X. Wang, C. Wang, *J. Phys. Chem. C* **112**, 11645–11649 (2008)
14. W.B. Soltan, M. Mbarki, S. Ammar, O. Babot, T. Toupance, *J. Mater. Sci.* **26**, 1612–1618 (2015)
15. W.B. Soltan, M. Mbarki, S. Ammar, O. Babot, T. Toupance, *Opt. Mater.* **54**, 139–146 (2016)
16. W.B. Soltan, M. Mbarki, R. Bargougui, S. Ammar, O. Babot, T. Toupance, *Opt. Mater.* **58**, 142–150 (2016)
17. S.V. Manorama, C.V.G. Reddy, V.J. Rao, *Nanostruct. Mater.* **11**, 643–649 (1999)
18. B. Cheng, J.M. Russell, W. Shi, L. Zhang, E.T. Samulski, *J. Am. Chem. Soc.* **126**, 5972 (2004)
19. F. Du, Z. Guo, G. Li, *Mater. Lett.* **59**, 2563 (2005)
20. S. Fujihara, T. Maeda, H. Ohgi, E. Hosono, H. Imai, S.H. Kim, *Langmuir* **20**, 6476 (2004)
21. H. Yang, X. Song, X. Zhang, W. Ao, G. Qiu, *Mater. Lett.* **57**, 3124 (2003)
22. Y. Liu, F. Yang, X. Yang, *Colloid Surf. A* **312**, 219–225 (2008)
23. J. Pena, J. Perez-Pariente, M. Vallet-Regi, *J. Mater. Chem.* **13**, 2290–2296 (2003)
24. D. Davazoglou, *Thin Solid Film* **302**, 204 (1997)
25. H.M. Rietveld, *J. Appl. Crystallogr.* **2**, 65 (1969)
26. E. Barsoukov, J.R. Macdonald, in *Impedance Spectroscopy Theory, Experiment, and Applications*, 2nd edn. (Wiley, Hoboken, 2005), pp. 1–20
27. J. Rodriguez Carjaval, in *XVth Congress International Union of Crystallography, proceedings of the satellite meeting on powder diffraction, Toulouse*, p. 199
28. P. Kirszensztejn, A. Tolinska, R. Przekop, *J. Therm. Anal. Calorim.* **95**, 93 (2009)
29. S.B. Ogale, R.J. Choudhary, J.P. Buban, S.E. Lofland, *Phys. Rev. Lett.* **91**, 077205 (2003)
30. N. Jiamiao, X. Zhao, J. Zhao, *Surf. Coat. Technol.* **206**, 4356 (2012)
31. K. Melghit, K. Bouziane, *J. Am. Ceram. Soc.* **90**, 2420–2423 (2007)
32. V. Stengl, T.M. Grygar, *Int. J. Photoenergy* doi:10.1155/2011/685935 (2011) Article ID 685935
33. G. Yang, Z. Yan, T. Xiao, *Appl. Surf. Sci.* **258**, 8704–8712 (2012)
34. R. Bargougui, A. Oueslati, G. Schmerber, C. Ulhaq-Bouillet, S. Colis, F. Hlel, S. Ammar, A. Dinia, *J. Mater. Sci. Mater. Electron.* **25**, 2066 (2014)
35. N. Tawichai, K. Sutjarittangtham, T. Tunkasiri, K. Pengpat, G. Rujijanagul, J. Wang, *Ceram. Int.* **39**, S145–S148 (2013)
36. H. Rahmouni, M. Smari, B. Cherif, E. Dhahrib, K. Khirouni, *Dalton Trans.* **44**, 10457 (2015)
37. A. Zaafour, M. Megdiche, M. Gargouri, *J. Alloys Compd.* **584**, 152 (2014)
38. M. Sassi, A. Bettaibi, A. Oueslati, K. Khirouni, M. Gargouri, *J. Alloys Compd.* **649**, 642–648 (2015)
39. S. Nasri, M. Megdiche, M. Gargouri *Physica B.* **451**, 120–127 (2014).
40. N. Bouazizi, F. Ajala, A. Bettaibi, M. Khelil, A. Benghnia, R. Bargougui, S. Louhichi, L. Labiadh, R. Benslama, B. Chaouachi, K. Khirouni, A. Houas, A. Azzouz, *J. Alloys Compd.* **656**, 146–153 (2015)
41. R. Zhou, A. Hierlemann, K.D. Schierbaum, K.E. Geckeler, *W. Go, Sens. Actuators B* **25**, 443–447 (1995)
42. H. Rahmouni, A. Dhahri, K. Khirouni, *J. Alloys Compd.* **591**, 259–262 (2014)
43. R.S. Meenakshi Dult, S. Kundu, R. Murugavel, N. Punia, *Kishore. Physica B* **452**, 102–107 (2014)
44. S. Nasri, M. Megdiche, M. Gargouri, *Ionics* **21**, 67–78 (2015)